RESEARCH ARTICLE | AUGUST 06 2025

The effect of streaks on the breakup of Kelvin–Helmholtz rolls in a geometry-induced laminar separation bubble

E. Canepa ; A. Crivellini ; M. Dellacasagrande ; A. Ghidoni ; G. Noventa

Physics of Fluids 37, 084109 (2025)
https://doi.org/10.1063/5.0274917

Physics of Fluids ARTICLE pubs.aip.org/aip/pof

The effect of streaks on the breakup of Kelvin–Helmholtz rolls in a geometry-induced laminar separation bubble

Cite as: Phys. Fluids **37**, 084109 (2025); doi: 10.1063/5.0274917
Submitted: 9 April 2025 · Accepted: 1 July 2025 ·
Published Online: 6 August 2025

View Online Export Citation CrossMark

E. Canepa,[1] A. Crivellini,[2] M. Dellacasagrande,[1,a)] A. Ghidoni,[3] and G. Noventa[3]

AFFILIATIONS

[1]DIME, University of Genoa, Genoa 16145, Italy
[2]DIISM, Polytechnic Marche University, Ancona 60131, Italy
[3]DIMI, University of Brescia, Brescia 25123, Italy

[a)]Author to whom correspondence should be addressed: matteo.dellacasagrande@edu.unige.it

ABSTRACT

This study investigates the influence of boundary layer streaks on the transition process of a geometry-induced laminar separation bubble (LSB). High-fidelity numerical simulations of the T3L test case, proposed by the European Research Community on Flow, Turbulence and Combustion, were performed. The resulting dataset describes a flat plate boundary layer under varying Reynolds numbers and free-stream turbulence levels and was analyzed using Dynamic Mode Decomposition (DMD). The DMD algorithm identifies the most amplified streamwise and spanwise wavelengths within the LSB and enables comparison with those of pre-transitional streaky structures perturbing the boundary layer. Under non-zero free-stream turbulence, elongated streaks develop in the attached boundary layer and shorten the bubble length. The presence of alternating high- and low-speed streaks in the cross-flow direction induces wall-normal oscillations of the separated shear layer, with a spanwise wavelength matching the streak spacing. Nevertheless, the strongest instability detected by the DMD analysis emerges farther downstream, where Kelvin–Helmholtz (K–H) rolls undergo breakdown. Both sinuous and varicose-like instabilities of the K–H structures were observed at the streamwise location corresponding to the highest disturbance growth, involving all three velocity components. The most amplified DMD modes captured a spanwise wavelength matching the streak spacing, characterizing the instability of the K–H rolls. Furthermore, these modes revealed the formation of regions of elevated streamwise vorticity associated with the unstable rolls, which enhances their distortion and subsequent breakdown. Analysis of the vorticity transport equation indicates that laminar streaks within the LSB reinforce the streamwise vorticity field, thereby promoting the instability and breakup of the K–H rolls.

I. INTRODUCTION

The detachment of the boundary layer from a solid surface may occur in the case of constant or streamwise varying pressure gradient,[1,2] high angles of attack,[3] or geometry discontinuity, such as forward/backward facing steps.[4] When the shear layer transitions to turbulence and is reattached to the wall, a laminar separation bubble (LSB) forms.[5] The growth of disturbances in a laminar separation bubble is typically driven by the Kelvin–Helmholtz (K–H) instability.[6] The convective growth of fluctuations leads to the shear layer roll-up and the formation of spanwise vortices, which cause momentum transfer toward the wall[7] and high levels of turbulence production.[8] Turbulence generation is due to the combination of Reynolds stresses caused by K–H rolls with the highly inflectional velocity profile in the laminar separation bubble. The 3D breakdown of the vortex pairs finally leads to the turbulent state of the boundary layer.[1] The statistical and dynamic behavior of a laminar separation bubble is strongly influenced by changes in the Reynolds number, the free-stream turbulence intensity (Tu) level, and the pressure gradient.[9,10]

For free-stream turbulence levels higher than about 1%, streaky structures may form in the attached boundary layer prior to the separation position.[11] If streak breakup statistically occurs earlier than boundary layer separation, the reversed flow region is no longer observed and the so-called bypass transition takes place.[12] The secondary instability of streaky structures indeed drives the formation of turbulent spots within the boundary layer, which then merge, causing transition to turbulence.[13,14] Depending on the free-stream turbulence level and the Reynolds number, streaks may propagate within the separated shear layer[8,15] without necessarily suppressing the laminar separation bubble. In such a flow configuration, flow features typical of separation induced transition and bypass one interact with each other.[16] Streaky structures perturb the K–H rolls while enhancing their instability process and their successive breakdown.[8] Simoni *et al.*[17] have studied the response of a flat plate laminar separation bubble to Reynolds number and free-stream turbulence under the effect of streamwise varying pressure gradient. The growth rate of disturbances in the fore part of an LSB has been found to show algebraic and exponential trends depending on the free-stream turbulence level and the Reynolds number. The authors speculated that streaky structures perturbed the BL in the case of moderate free-stream turbulence, causing the growth of streamwise fluctuations. Istvan *et al.*[18] have observed the propagation of streaky structures in an airfoil LSB for Tu levels below 2%. The presence of laminar streaks indicated an onset of bypass transition upstream of the separation position, provoking a highly three-dimensional shear layer roll-up. Sengupta and Tucker[8] have studied the cumulative effects due to forced oscillation and free-stream turbulence on a flat plate BL subjected to the pressure gradient typical of low-pressure turbine blades. Under the influence of free-stream turbulence, streamwise streaks have been seen to provoke spanwise modulation of K–H rolls, thus shortening the laminar separation bubble with respect to zero free-stream turbulence conditions. Aniffa *et al.*[19] have studied geometry- and pressure-induced LSBs for different Tu levels. In the case of pressure-induced laminar separation bubbles, streaks have been found to distort the 2D K–H rolls, eventually leading to the formation of a three-dimensional Λ-like structure. It has been shown that the boundary layer streaks do not bypass or suppress the primary K–H instability but distort the 2D roll structure, even in the case of enhanced levels of free-stream turbulence.

The aforementioned works indicate that competing transition mechanisms coexist within a laminar separation bubble, depending on Reynolds number and Tu level,[20,21] with streaky structures possibly affecting the shear layer stability characteristics. The stability properties of a laminar separation bubble have been widely studied by means of linear stability theory (LST).[19,22–26] LST has been shown to correctly predict the most unstable wavelengths characterizing the K–H instability under different levels of free-stream turbulence. Besides LST, data-driven techniques such as Spectral Proper Orthogonal Decomposition (SPOD) and Dynamic Mode Decomposition (DMD) have been used to derive the most unstable boundary layer modes from numerical and experimental data.[27–32] Among others, Weiss *et al.*[28] have used SPOD to study the low-frequency breathing motion of a turbulent separation bubble. Low-order models retaining the contribution of the first SPOD mode for the lowest frequencies have been shown to well capture the contraction and expansion modes of the separation bubble. Wu *et al.*[32] applied DMD on high-fidelity numerical data describing a flat plate laminar separation bubble. DMD has been shown to capture both low- and high-frequency (K–H) modes. Wu *et al.*[32] have computed DMD considering the entire streamwise extension of the computational domain. As observed by the authors, the resulting modes were all stable or slightly unstable, due to the statistically saturated state of the flow. Successively, Wang and Shoele[29] proposed a modification of the classic DMD procedure aimed at characterizing the transient behavior of a laminar separation bubble. A sparsification network gathering response modes based on an energy-like index has been used for space–time localization of unstable modes within a separated boundary layer.

In the present work, DMD was used to extract the most unstable modes from high-fidelity numerical simulation data describing geometry-induced laminar separation bubbles forming at different Reynolds numbers and free-stream turbulence levels. The formation of streaky structures in the separated shear layer for the present cases allowed us to study their role in defining the unstable flow pattern that led to shear layer transition. Streaks were found to enhance the distortion of the K–H rolls, thus shortening the length of the laminar separation bubble. The paper is organized as follows: Secs. II and III describe the case study and the numerical setup. The DMD mathematical framework is provided in Sec. IV. Sections V and VI report the main results and concluding remarks.

II. CASE STUDY

The current test case is a part of a larger database concerning Implicit Large Eddy Simulations (ILES) of geometry-induced laminar separation bubbles evolving on a semi-infinite flat plate with a rounded leading-edge corner. More specifically, the T3L test case of the European Research Community on Flow, Turbulence and Combustion (ERCOFTAC) suite[33] was considered for different Reynolds numbers (Re), based on the leading-edge diameter D and the free-stream velocity u_{ref}, and different free-stream turbulence levels (Tu). In this study, the response of the LSB to variations in turbulence integral length scale was not investigated, as previous works[11] reported its effects to be minor compared to those of turbulence intensity. Further research is needed to assess the potential influence of turbulence length scale. The flow conditions discussed in the present work are summarized in Table I. The case labels are the same as those of the ERCOFTAC suite.[33]

III. NUMERICAL SETUP

Implicit Large Eddy Simulations (ILES) with high-order discontinuous Galerkin (dG) discretization of the Incompressible Navier–Stokes (INS) equations (see the Appendix) are performed in this work.[34,35] The high potential of the dG discretizations for the under-resolved simulation of turbulent flows has been demonstrated in the literature for those moderate Reynolds number conditions where Reynolds-averaged Navier–Stokes (RANS) equations typically fail to provide an accurate prediction of the flow, e.g., separated flows.[36] High-order dG introduces dissipation and dispersion of high wave numbers, while at low and medium wave numbers the dissipation error is reduced. The dissipation error, increasing at the smallest under-resolved scales, resembles a high wave-number filter that mimics the role of a sub-grid scale model, whereas, where the flow is fully resolved, a very small amount of dissipation is introduced. Then, the dG method does not introduce any nonphysical sub-grid dissipation in the regions where the flow is fully resolved, such as in the laminar flow regions, for instance. ILES of several canonical flows have been performed with the same solver used in this work by Franciolini *et al.*,[35] Franciolini *et al.*,[37] and Bassi *et al.*[34] Similarly to standard finite

TABLE I. Summary of analyzed flow cases.

Case	T3L0L	T3L5	T3L4L	T3L3	T3L6
Re	1725	1725	1725	3450	6900
Tu	0	2.3	5.6	2.3	2.3

element (FE) approaches, dG schemes use polynomial spaces of degree k to approximate the solution, corresponding to DoFs $= \prod_{i=1}^{3}(k+i)/i$ degrees of freedom per element.

Figure 1 shows the computational domain, where D is the diameter of the plate leading edge (LE), L_x is the distance between the leading edge and the inlet boundary, and (D_x, D_y, D_z) are the dimensions of the computational domain. The domain extension on the x–y plane is $D_x = 28D$ and $D_y = 17D$, and it is extruded using 10 elements along the spanwise direction z, with $D_z = 2D$. The spanwise dimension of the domain was set according to Yang and Voke,[38] where a spanwise dimension of $D_z = 4D$ demonstrated less than 5% difference in terms of first- and second-order statistics compared to $D_z = 2D$. A free-stream velocity u_∞ was assigned at the inlet, while a pressure condition was set at the outlet. Periodic boundary conditions were applied at the spanwise boundaries. All the simulations were carried out on a hybrid computational mesh of 38 320 elements with quadratic edges. The near-wall hexahedral mesh is uniform in the spanwise direction. The unstructured mesh is coarsened moving away from the plate to reduce the computational cost of the simulations. The dimensional height of the first element at the wall is $10^{-2}\,D$ over the entire plate surface, with the mesh being refined at the leading edge, where the minimum grid element size in the streamwise direction is $2 \times 10^{-2}\,D$. The time integration was performed using linearly implicit Runge–Kutta schemes of the Rosenbrock type, specifically the three-stage and third-order ROS3P scheme[39] with time step $0.01D/u_{ref}$. To reduce computational costs, a Matrix-Free implementation of the Generalized Minimal Residual method was employed, coupled with a p-MultiGrid preconditioner to minimize memory usage.[35] All the simulations were carried out as unsteady ones starting from the steady-state solution with degree $k = 3$. Each steady simulation of the pre-processing with $k = \{0, 1, 2, 3\}$ is initialized with the steady-state solution with a lower by one degree, while the unsteady simulations were carried out for 20 convective times defined as D/u_{ref} with $k = \{3, 4, 5\}$ until the use of the maximum degree $k = 6$. After reaching a statistically steady condition after 20 convective times, 50 convective times were considered for the computation of flow statistics. First- and second-order statistics were averaged both in time and in the spanwise direction in order to improve statistical convergence. The number of degrees of freedom of all the simulations is DoFs $= 3\,218\,880$.

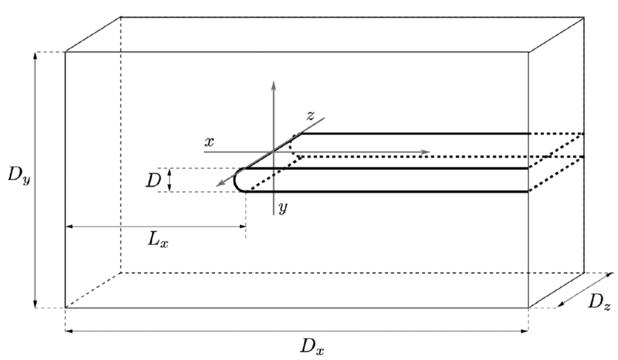

FIG. 1. Computational domain, where (x, y, z) are the streamwise, cross-wise, and spanwise directions, D is the diameter of the leading edge of the plate, L_x the distance of the leading edge from the inflow boundary, and (D_x, D_y, D_z) the domain dimensions.

The numerical setup was the same as Bassi *et al.*,[34] Cimarelli *et al.*,[36] and Franciolini *et al.*[35] Particularly, Bassi *et al.*[34] demonstrated the agreement between the numerical results and the experiments of the ERCOFTAC suite[33] in terms of the spanwise- and time-averaged velocity and root mean square profiles at different locations along the plate. Franciolini *et al.*[35] also demonstrated the spatial convergence of such BL quantities with different degrees of the provided solution. Figures 2 and 3 illustrate the spanwise- and time-averaged profiles of streamwise velocity and of the root mean square of streamwise velocity fluctuations along the plate in all cases in comparison with the available experiments of the ERCOFTAC suite.[33] All the streamwise

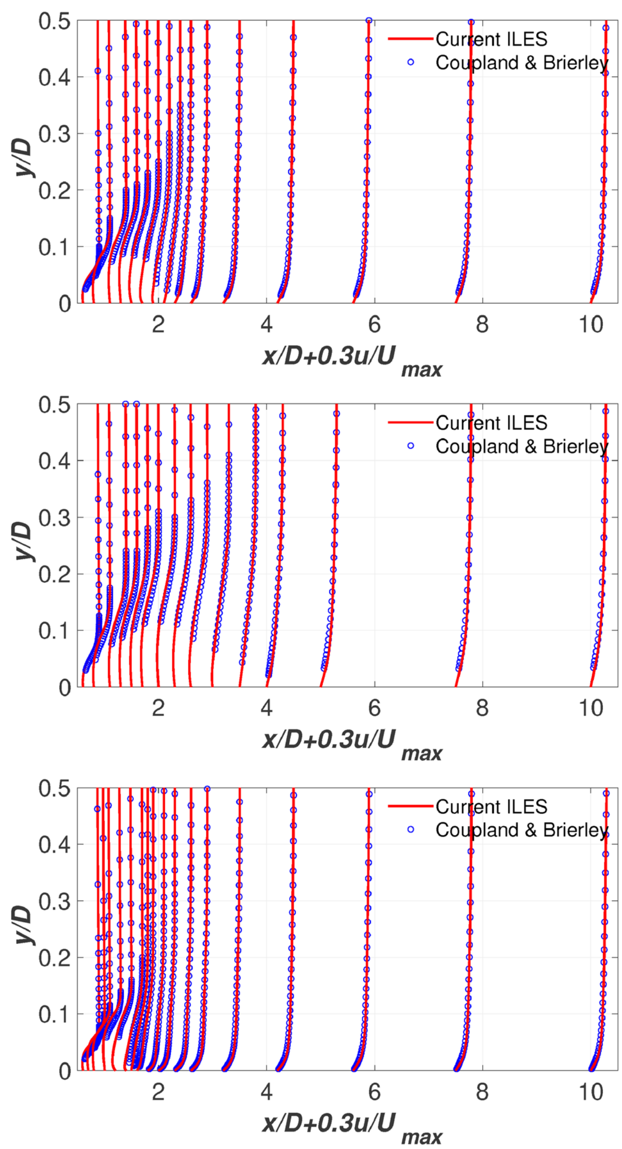

FIG. 2. Spanwise- and time-averaged streamwise velocity profiles in the cross-wise direction along the plate in the T3L3 (top), T3L5, and T3L6 (bottom) cases in comparison with the experiments of the ERCOFTAC suite.[33]

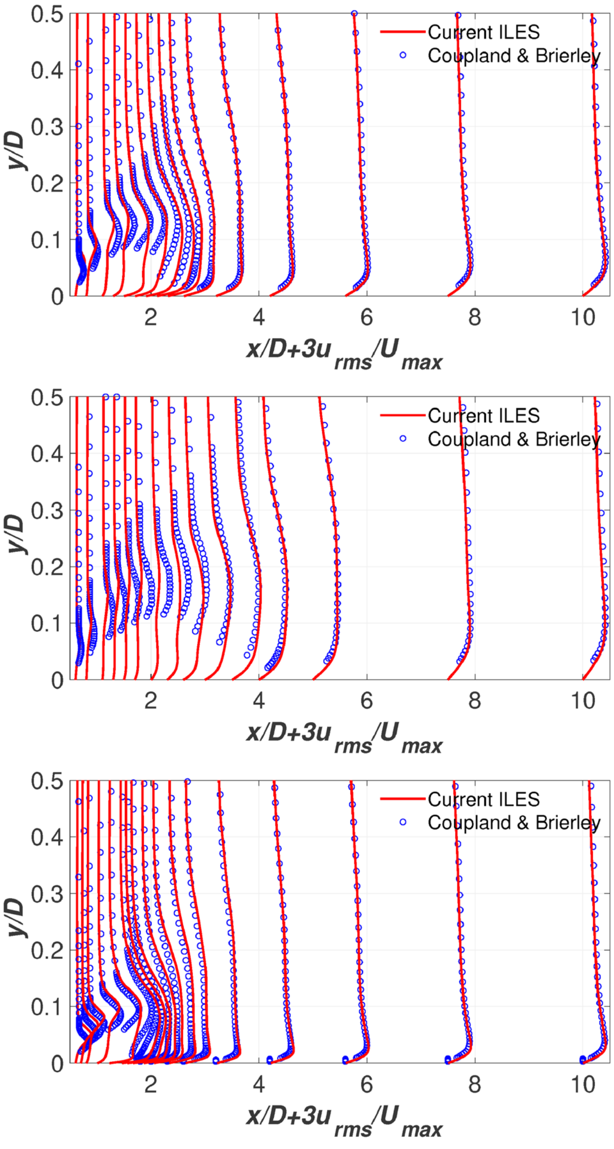

FIG. 3. Root mean square of the streamwise velocity fluctuations profiles in the cross-wise direction along the plate in the T3L3 (top), T3L5, and T3L6 (bottom) cases in comparison with the experiments of the ERCOFTAC suite.[33]

velocity profiles are in agreement with the experiments, and small differences in the free-stream are due to a different blockage ratio between the experimental setup and the computational domain. The root mean square profiles show non-negligible differences near the wall within the recirculating flow region, and this is ascribed to a lack of resolution in the experimental data, which are measured with a single hot-wire probe.[38] Downstream of the reattachment point, the agreement of the root mean square of the streamwise velocity increases again. Figures 4 and 8 illustrate the spanwise- and time-averaged skin friction coefficient and the shape factor distribution along the plate in all cases in comparison with the available experiments of the

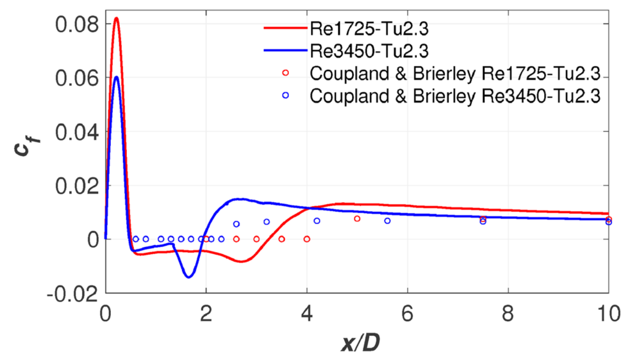

FIG. 4. Spanwise- and time-averaged skin friction coefficient distribution along the plate in comparison with the experiments of the ERCOFTAC suite.[33]

ERCOFTAC suite.[33] A good agreement is observed between the experiments and the present numerical simulations.

IV. DMD MATHEMATICAL FRAMEWORK

The Dynamic Mode Decomposition (DMD) was introduced in the fluid dynamic community by Schmid.[40] DMD is a dimensionality reduction data-driven technique for the analysis of numerical and experimental data. In its classic formulation, DMD is applied to high-dimensional data to extract the underlying coherent patterns and then isolate their dynamic behavior.[41]

From the mathematical point of view, the DMD algorithm gives the best linear approximation of a dynamical system for which a set of N observations is provided by means of experiments or numerical simulations. Considering the state $\mathbf{x}$ (flow record) of a given system, the DMD algorithm produces a low-rank eigendecomposition of the matrix A that optimally fits the measured data in a least-squares sense, so that

$$err = ||\mathbf{x}_{k+1} - A\mathbf{x}_k||_2 \tag{1}$$

is minimized across all the observations, i.e., $k = 1, 2, 3, \ldots, N-1$. To minimize the approximation error (1) across all snapshots, it is possible to arrange the N flow records into two large data matrices[42]

$$X = \begin{bmatrix} | & | & & | \\ x_1 & x_2 & \cdots & x_{N-1} \\ | & | & & | \end{bmatrix}, \tag{2}$$

$$X' = \begin{bmatrix} | & | & & | \\ x_2 & x_3 & \cdots & x_N \\ | & | & & | \end{bmatrix}, \tag{3}$$

where each column of X and X' consists of the three velocity components. According to Eq. (1), A is computed as $A = X'X^+$, where X^+ is the Moore–Penrose pseudo-inverse of X. The DMD modes ϕ and the complex eigenvalues λ are then obtained from the eigensolution of A once projected into the singular vectors of X. Then, the state $\mathbf{x}_k$ at time t_k can be expressed in terms of the eigenvalues λ and eigenvectors (i.e., the DMD modes) ϕ of A as

$$\mathbf{x}_k = \sum_{j=1}^{N} \phi_j \lambda_j^k b_j = \Phi\Lambda^k B, \tag{4}$$

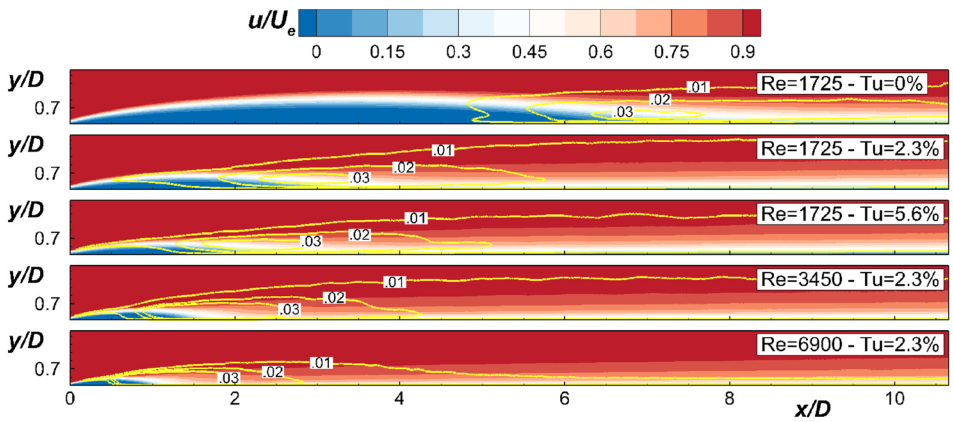

FIG. 5. Time-mean streamwise velocity for different Reynolds numbers and Tu levels. Velocity is scaled with its free-stream value U_e. Iso-contour lines of turbulent kinetic energy scaled with the external velocity TKE/U_e^2=0.01, 0.02, and 0.03 are shown (yellow colored lines).

where B is the amplitude of $\mathbf{x}(t_1)$ in the eigenvector space. The real part of the complex λ_j provides the growth/decay rate of the jth wavelength retained by the corresponding imaginary part. Therefore, a set of growing/decaying Fourier modes can be obtained by the application of DMD to the current database, capturing the most unstable flow scales within a laminar separation bubble.[43–47]

In the present work, DMD was applied on numerical data describing the leading edge (LE) separation of a flat plate boundary layer for different free-stream turbulence levels and Reynolds numbers. Data were stacked in the matrices X and X' [Eqs. (2) and (3)] so that each column contains data at a fixed streamwise position. The wall-normal and spanwise coordinates vary instead with the row index. Accordingly, the DMD eigenvalues are representative of streamwise wavelengths growing/decaying in the mean flow direction, whereas DMD modes have the shape of cross-flow (y–z)-planes. Furthermore, DMD was computed in the x-direction for each snapshot independently, and then the results were averaged over time to improve the statistical convergence of the data. Then, the current procedure captures the convective unstable modes in an LSB that are typically linked to the occurrence of the K–H instability[48] and, under non-null free-stream turbulence, to the propagation of streaky structures.[49]

In order to provide the local characterization of the most unstable modes of the LSB, the DMD domain has been gradually extended in the streamwise direction. As the domain extension increases, the number of columns of X and X' also increases, while the number of rows remains constant. Consequently, the dimension of the resulting modes is not changed. The choice of considering a streamwise window with increasing size instead of a moving window with fixed dimension is based on previous authors' work where the currently adopted method was seen to preserve sensitivity to localized instability,[48,50] while providing less noisy DMD results as well as avoiding iterating on the moving window size. The size of the chosen window indeed determines the largest observable wavelength. Using a streamwise window of increasing length ensures that a sufficiently large domain is considered upon reaching the region of linear amplification of fluctuations near the bubble maximum displacement. The initial DMD domain extends from the LE up to $x/D = 0$, namely, the end of the rounded leading edge of the plate, and it is further extended up to the end of the numerical domain. To maintain a constant increment step for the DMD domain, the simulation data were first interpolated onto a uniform structured grid along the x-direction. The number of snapshots considered for the DMD analysis varied for the different cases, covering about 300 characteristic time scales defined as D/u_∞.

V. RESULTS

A. Statistical response of the laminar separation bubble to Re and *Tu* level variation

Figure 5 illustrates the spatial distributions of the non-dimensional time-mean streamwise velocity at different Re and Tu levels. Iso-contour lines of the turbulent kinetic energy (TKE) scaled with the local free-stream velocity (U_e) are also shown. As expected, the size of the laminar separation bubble decreases as the Reynolds number and the Tu level increase.[51] Both the height and the length of the reversed flow region reduce, with the shear layer shifting closer to the plate surface. However, the boundary layer consistently separates near the junction between the rounded leading edge and the flat portion of the plate, regardless of Re and the Tu level. Note that the case with zero free-stream turbulence exhibits a significantly longer separation compared to cases with a non-null turbulence level.

The highest values of TKE/U_e are seen near the maximum displacement of the bubble, where K–H rolls are known to occur.[18] Successively, their instability and breakdown cause the turbulent transition and reattachment of the boundary layer.[18,52] Evidence of such phenomena will be provided in Sec. V B (see, e.g., Figs. 10 and 11). As Re and Tu level increase, higher levels of TKE are seen in the fore part of the laminar separation bubble. As shown in the following, higher levels of TKE are due to the formation of streaky structures in the boundary layer under the influence of free-stream turbulence.[49]

Figure 6 compares the length of the laminar separation bubbles shown in Fig. 5 to the data reported in the literature works of Coupland and Brierley,[43] Palikaras *et al.*,[44] Yang and Voke,[38] Langari and Yang,[45] and Lamballais *et al.*[46,47] These latter works are indeed concern with the same flow cases analyzed in this work. Details on the current separation and reattachment positions are reported in Table II. Figure 6 also shows fitting curves providing the length of LSBs as a function of Tu for the three Reynolds numbers tested. The function $L_b/D = KTu^m$ was used to interpolate the data, where $K = [3.38, 1.77, 1.17]$ and $m = [-0.30, -0.27, -0.29]$ for the three Reynolds numbers, respectively. The coefficients were calibrated considering ten additional flow cases that are not presented here. Note that the fitting curve for $Re = 3450$ well matches the DNS data of Lamballais *et al.*[46,47] and the experimental ones by Palikaras *et al.*[44] at

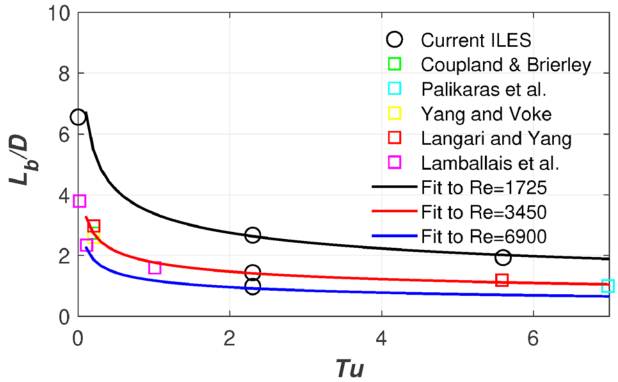

FIG. 6. Spanwise and time-mean length of the separation bubble, L_b/D. Solid lines represent the interpolation function $L_b/D = KTu^m$ with $K = 3.38$, 1.77, 1.17 and $m = -0.30, -0.27, -0.29$. Literature data from Coupland and Brierley,[43] Palikaras *et al.*,[44] Yang and Voke,[38] Langari and Yang,[45] and Lamballais *et al.*[46,47] are shown for comparison.

$Tu = 7\%$. The data shown in Fig. 6 highlight the consistency of the present simulations with previous experimental and numerical results.

Figure 7 reports the streamwise variation of the peak value of the local root mean square (rms) profile of both the streamwise (u_{rms}) and the wall-normal (v_{rms}) fluctuating components, which are scaled with the external velocity U_e. Streamwise fluctuating velocity is known to be affected by bubble breathing and flapping,[53] as well as by the propagation of streaky structures in the separated shear layer,[16,18] see, e.g., the elongated structures forming downstream of the LE in Fig. 10(a) for non-null Tu levels. Accordingly, u_{rms}/U_e shows higher values than v_{rms}/U_e in the fore part of the laminar separation bubble. It has to be noted that two different trends characterize the u_{rms}/U_e distributions in the fore part of the LSB, i.e., upstream of the maximum peak location. A quasi-logarithmic trend is observed downstream of the separation position while the growth rate significantly increases approaching the maximum bubble height (see the inset plot in Fig. 7). As discussed by Istvan *et al.*[18] and Simoni *et al.*,[17] streaky structures are responsible for the quasi-logarithmic growth of fluctuations in the fore part of the separated shear layer, while K–H instability causes the exponential growth of both u_{rms}/U_e and v_{rms}/U_e when approaching the maximum displacement of the bubble. According to previous studies on pressure-induced LSBs,[17,18] the Reynolds number shows the greatest effects on the growth rate (σ) of K–H-related fluctuations, which drive the growth of v_{rms}/U_e in the rear part of the bubble. In the current work, σ has been estimated according to Sarmast *et al.*[54] as

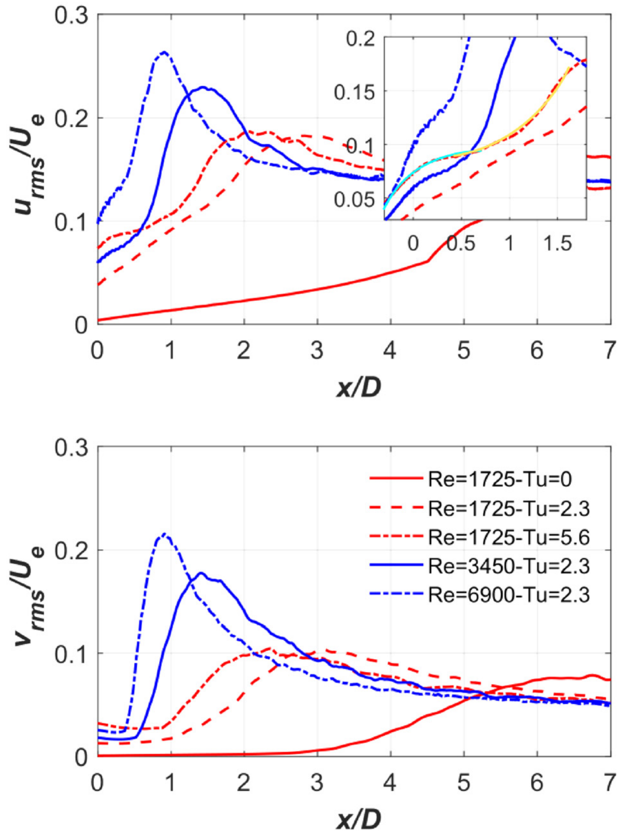

FIG. 7. Root mean square of the streamwise (top) and wall-normal (bottom) velocity fluctuations. The quasi-logarithmic and exponential trends of u_{rms}/U_e are highlighted in the top plot with green and orange curves, respectively, for the case Re = 1725 to Tu = 2.3%.

$$\sigma = \frac{\ln(v'_{rms}/U_e)_{sat} - \ln(v'_{rms}/U_e)_0}{(x/D)_{sat} - (x/D)_0}, \quad (5)$$

where subscripts "sat" and "0" refer to the position of saturation of v_{rms} and the onset of exponential growth, respectively. The values obtained for the present cases are reported in Table III. The growth of v_{rms}/U_e, which is mostly related to the onset of the K–H instability process, increases with *Re*, while the *Tu* level has a lower effect in this sense. It should also be noted that the highest peak of v_{rms}/U_e increases with *Re*, while the same peak values of v_{rms}/U_e are observed across different *Tu* levels.[49] This response of the maximum rms of fluctuations to changes in the Reynolds number differs from the behavior typically

TABLE II. Separation (x_S), reattachment (x_R), and maximum P_k (x_P) location.

Re	*Tu* (%)	x_S/D	x_R/D	$(x_P - x_S)/(x_R - x_S)$
1725	0	0.0	6.57	0.89
1725	2.3	0.0	2.69	0.88
1725	5.6	0.0	1.91	0.87
3450	2.3	0.0	1.42	0.8
6900	2.3	0.0	0.95	0.78

TABLE III. Growth rate (σ) of K–H related fluctuations computed according to Eq. (5).

Case	T3L0L	T3L5	T3L4L	T3L3	T3L6
Re	1725	1725	1725	3450	6900
Tu	0	2.3	5.6	2.3	2.3
σ	0.78	0.9	1.06	2.5	3.85

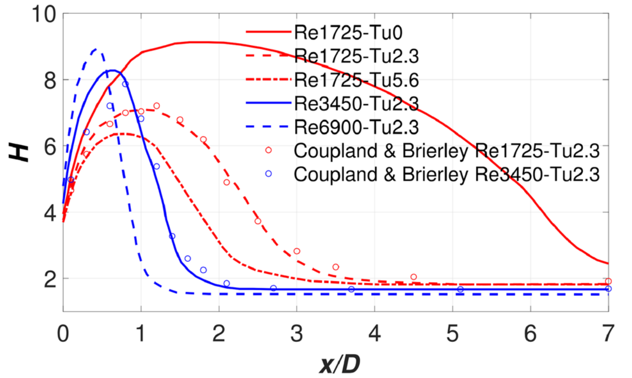

FIG. 8. Spanwise- and time-averaged shape factor of the BL in comparison with the experiments of the ERCOFTAC suite.[33]

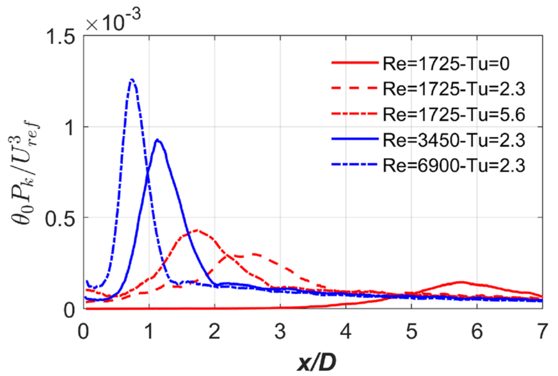

FIG. 9. Spanwise and time-mean non-dimensional local peak value of turbulent kinetic energy production.

observed in the case of pressure-induced LSBs, which exhibit an almost constant non-dimensional peak of fluctuations when varying both the Reynolds number and the Tu level.[51]

To illustrate the effects of the Reynolds number and free-stream turbulence on transition, as well as on the generation of turbulence within the LSB, Fig. 8 compares the shape factor (H) and Fig. 9 compares the local peak value of turbulent kinetic energy production (P_k) in the boundary layer. This latter corresponds to the maximum P_k value computed at each streamwise position across the boundary layer thickness. The peak of the shape factor (top plot), which indicates the mean transition position, shifts upstream as Re and the Tu levels increase. Furthermore, the transition length, defined as the distance between the peak of H and the point of minimum saturation, decreases with increasing values of these flow parameters. Note that at $Tu = 0$, the boundary layer remains transitional at $x/D = 7$, whereas for the other cases, i.e., for $Tu > 0$, transition completion occurs at $x/D < 4$. The modification of the shape factor peak is linked to the changes in the time-mean structure of the LSB. More specifically, the reversed flow magnitude plays a key role in determining the maximum value of this quantity, being directly linked to the local value of the BL momentum thickness. Differently from what is typically observed in pressure-induced LSB,[51] the peak of H slightly increases with Re. This is a consequence of the modification of the time-mean structure of the BL at the detachment position, which always occurs at the junction between the LE and the flat portion of the plate.

The P_k distributions (bottom plot) are presented in non-dimensional form, using the free-stream velocity and the momentum thickness at the separation position as scaling quantities. Turbulence production is defined as $P_k = -u_i' u_j' \frac{\partial \bar{u}_i}{\partial x_j}$, where u' and $\bar{u}$ represent the fluctuating and time-mean velocity components, respectively. As the Reynolds number and Tu level increase, the peak value of P_k also increases, with its location shifting upstream. The Reynolds number has the most significant influence on the intensity of local turbulence production, with higher P_k values observed further upstream at higher

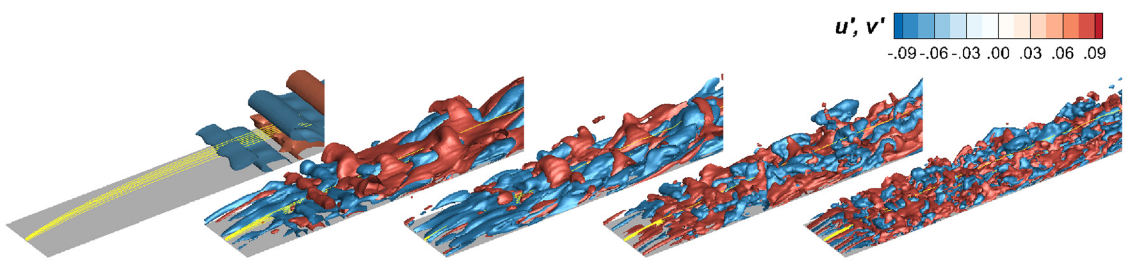

(a) Iso-surfaces of streamwsie fluctuations $u' = \pm 0.08$ m/s colored by u'.

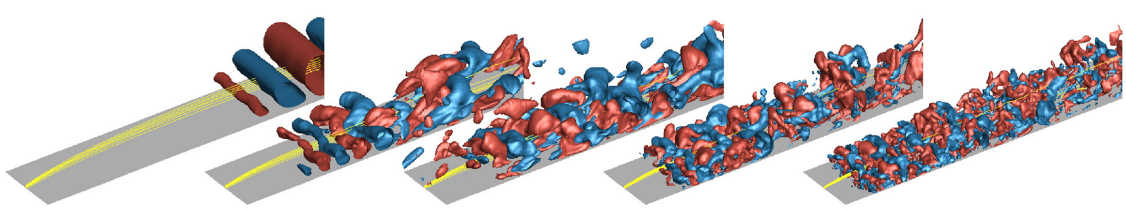

(b) Iso-surfaces of wall-normal fluctuations $v' = \pm 0.08$ m/s colored by v'.

FIG. 10. Instantaneous flow fields for variable *Re* and *Tu*. Iso-contour lines of time-mean streamwise velocity are shown with yellow color. Data are plotted for $0 < x/D < 6$. From left to right: $Re = 1750$ to $Tu = 0$, $Re = 1750$ to $Tu = 2.3$, $Re = 1750$ to $Tu = 5.6$, $Re = 3450$ to $Tu = 2.3$, and $Re = 6900$ to $Tu = 2.3$.

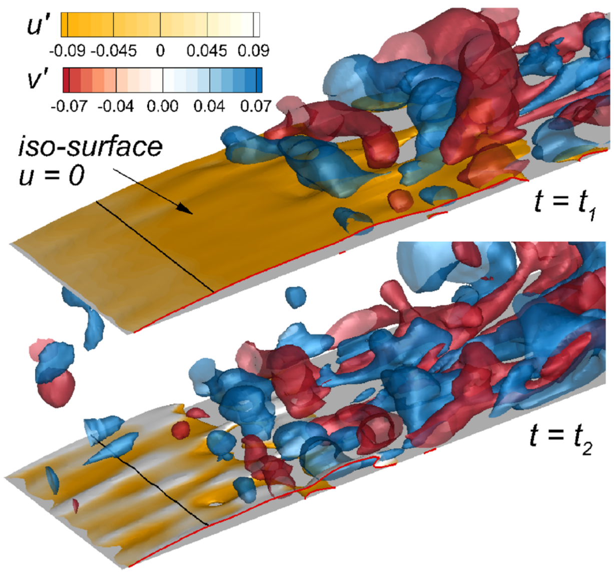

FIG. 11. Instantaneous flow records for the case $Re = 1750$ to $Tu = 5.6\%$. The iso-surface of wall-normal velocity fluctuations $v' = \pm 0.07$ m/s and the instantaneous iso-surface of zero streamwise velocity $u = 0$ colored by u' are shown. Black and red solid lines represent spanwise and streamwise cuts of the surface at $u = 0$, respectively.

Reynolds numbers. Since local turbulence production results from the interaction between turbulent stresses and the time-mean shear, the response to variations in Re is directly linked to changes in the time-mean structure of the boundary layer, with the disturbance level held constant. In contrast, varying the turbulence intensity alters the Reynolds stresses, while the local strain rate is expected to remain unchanged. The changes in the strain field induced by varying Re are

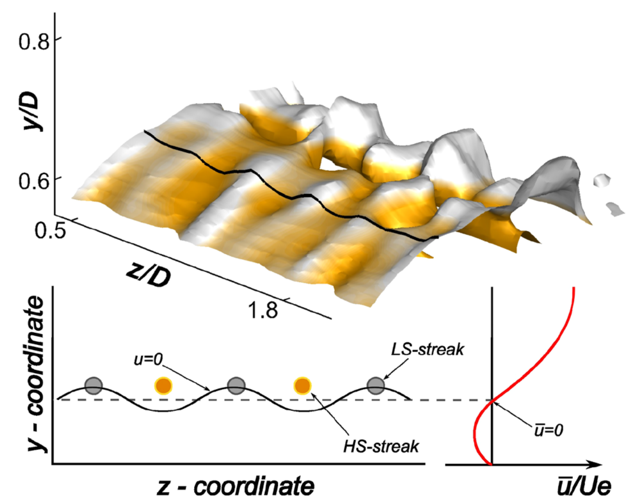

FIG. 12. Top: Iso-surface of $u = 0$ colored by u' for the case $Re = 1750$ to $Tu = 5.6$. The spanwise distribution of an iso-line at $u = 0$ (black line) is shown. Bottom: Schematic of the spanwise deformation of the recirculating flow region due to the propagation of high- and low-speed streaks.

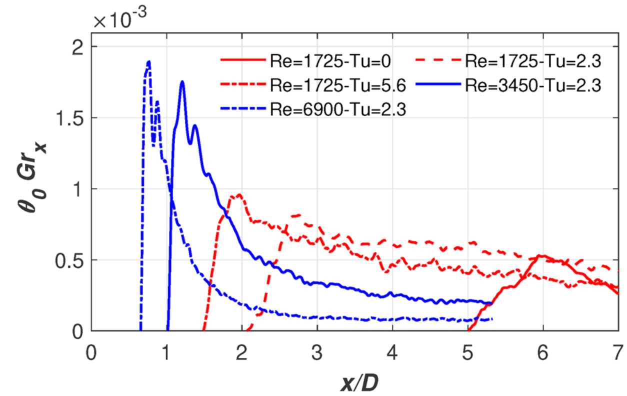

FIG. 13. Non-dimensional real part of complex DMD eigenvalues ($\theta_0 Gr_x$) plotted against axial coordinate.

found to have a stronger impact on turbulence production compared to those caused by changes in the Tu level. Table II presents the relative location of the maximum P_k value within the LSBs. This maximum is observed to shift upstream, closer to the separation position, as Re and the Tu level increase, indicating that turbulence production occurs in the upstream region of the LSB. For the current flow cases, the peak in turbulence production is associated with the formation and instability of K–H rolls. K–H rolls indeed generate high levels of Reynolds shear stresses, combined with significant spanwise vorticity. Their contribution to P_k is known to dominate within an LSB and is primarily concentrated near the bubble maximum height. In contrast, the contribution of streaks to P_k was found to be marginal, due to the local acceleration near the leading edge.

B. Dynamic response of a laminar separation bubble to flow parameter variation

To provide a qualitative view of the dynamics occurring within the LSB, exemplary snapshots are reported in Fig. 10 for the present cases. Iso-surfaces of the streamwsie (top) and the wall-normal (bottom) velocity fluctuations are shown. At $Tu = 0$ (left plots), high spanwise coherence of K–H rolls is observed, and velocity fluctuations in the separated shear layer are substantially negligible (see the top-left plot). The breakup to turbulence and transition were seen to occur further downstream for this specific flow case according to the shape factor distribution depicted in Fig. 8. As the Tu level and Re increase, elongated streaky structures develop in the boundary layer (top plots).

TABLE IV. Maximum peak of DMD non-dimensional growth rate, $\theta_0 Gr_{x,max}$, with its corresponding non-dimensional wavelength, $(\theta_0/l_x)_{Gr_{x,max}}$, and relative streamwise position.

Re	Tu (%)	$\theta_0 Gr_{x,max}$	$(\theta_0/l_x)_{Gr_{x,max}}$	$(x_{Gr_{x,max}} - x_S)/(x_R - x_S)$
1725	0	53×10^{-4}	0.0076	0.9
1725	2.3	81×10^{-4}	0.014	0.91
1725	5.6	96×10^{-4}	0.018	0.92
3450	2.3	175×10^{-4}	0.018	0.85
6900	2.3	190×10^{-4}	0.021	0.79

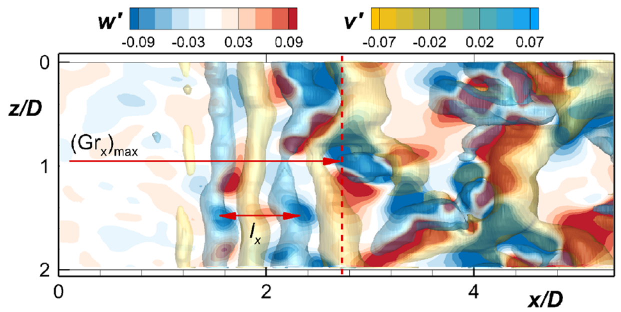

FIG. 14. Top view of instantaneous flow field for $Re = 1725$ to $Tu = 2.3\%$. Iso-surfaces at constant $v' = \pm 0.07$ m/s colored by v' are shown together with a contour plot of w' in a wall-parallel plane located at the centerline of spanwise vortices.

K–H rolls are seen to be rapidly distorted, and the formation of hairpin-like structures can be observed in Fig. 10. K–H rolls exhibit marked spanwise distortion yet close to the bubble maximum displacement, near the position where spanwise vortices originate. Both sinuous- and varicose-like distortions are observed. The former manifests as spanwise oscillation of the rolls, whereas the latter provokes their successive contraction and expansion. Also, the size of both streaks and K–H rolls reduces at higher Reynolds numbers.[16,55]

Figure 11 shows two instantaneous flow fields with the absence ($t = t_1$) and presence ($t = t_2$) of streaky structures in the separated BL. The case $Re = 1750$ to $Tu = 5.6\%$ is presented even though similar considerations can be applied to the other cases with non-null free-stream turbulence levels. The instantaneous shape of the recirculating flow region is highlighted by means of the iso-surface of zero instantaneous streamwise velocity ($u(t) = 0$), which is colored by its fluctuating component, i.e., $u(t)'$. At $t = t_1$ (top plot), when no streaks perturb the LSB, the separated shear layer shows a uniform distribution along the span, and spanwise coherence of the K–H rolls is observed. Instead, when streaks move downstream of the separation position ($t = t_2$, bottom plot), the 2D surface delimiting the reversed flow region is perturbed in the cross-flow direction with a spanwise scale that is the same as that of streaky structures (see the black line in the bottom frame). K–H rolls are seen to lose spanwise coherence, and they break up far upstream compared to the top plot. Consequently, the bubble length is reduced by about 30%. What is shown here indicates that under the influence of free-stream turbulence, streaks act to promote the instability of the separated shear layer, and the earlier breakup of the initially 2D rolls occurs.

To better elucidate how streaks cause 3D perturbation of the separated shear layer, Fig. 12 reports a scheme showing the effect of alternating high- and low-speed streaks on the instantaneous structure of the separation bubble. The top plot provides a perspective view of the separated shear layer, as depicted in Fig. 11 for $t = t_2$. The wall-normal coordinate has been stretched to offer a more detailed visualization of the shear layer. The spanwise perturbation of the iso-surface corresponding to $u(t) = 0$ is highlighted with a solid black line. According to the well-known Reynolds decomposition, the instantaneous streamwise velocity $u(t)$ can be expressed as the sum of the time-averaged and fluctuating components, i.e., $u(t) = \bar{u} + u'(t)$. Then, when $u'(t) = 0$ the instantaneous wall-normal position at which $u(t) = 0$ coincides with the wall-normal location where $\bar{u} = 0$. Differently, when streaks perturb the separated boundary layer, i.e., when $u'(t) \neq 0$, the time-averaged and fluctuating velocity components must have opposite signs to have $u(t) = 0$. Then, low-speed streaks ($u'(t) < 0$) induce a positive wall-normal displacement of the instantaneous zero-velocity line relative to the position where $\bar{u} = 0$ while high-speed streaks ($u'(t) > 0$) cause the instantaneous zero-velocity line to shift toward the plate. Streaks are therefore responsible for the spanwise perturbation of the separated shear layer, with a wall-normal amplitude that scales with the streak dimensions. According to the Reynolds decomposition reported above, the time-averaged value of the fluctuating component at a given spatial location, i.e., $\bar{u'}$, must be zero by definition. It follows that positive and negative values of u' occur at different time instants at fixed streamwise and wall-normal positions, being linked to the propagation of high- and low-speed streaks, respectively. It follows that the wall-normal location of the surface enclosing the recirculating flow region necessarily varies over time due to the presence of alternating streamwise streaks. Based on the observations in Figs. 11 and 12, the earlier breakup of an LSB observed with increasing Tu levels appears to be closely associated with an additional spanwise perturbation superimposed on the shear layer by the propagation of pre-transitional streaky structures.

To quantify the changes in the stability characteristics of an LSB with varying Reynolds number and Tu level, DMD was applied along the streamwise coordinate for the different cases to extract the most unstable streamwise and spanwise wavelengths. As detailed in Sec. IV, the DMD domain was progressively extended in the flow direction, and the most unstable mode was recorded for each extension of the analyzed region. According to the current method, DMD eigenvalues represent streamwise wavelengths that grow or decay in the flow direction, while the corresponding modes take the form of 2D cross-flow velocity distributions. Figure 13 shows the real part of the most unstable DMD eigenvalue for each streamwise extension of the DMD domain. It provides the growth rate (Gr_x) of the most unstable perturbation within the LSB. The corresponding imaginary part provides the associated streamwise wavelength (l_x), which was found to be equal to the wavelength of the K–H rolls at the position of the Gr_x peak. Its response to the flow parameter variation is synthesized in Table IV. Data shown in Fig. 13 show that Gr_x has a maximum peak for all Re and Tu levels, which moves upstream as Re and the free-stream turbulence increase. This is consistent with the anticipation of transition and the shortening of the laminar separation bubble, as shown in Fig. 5. Also, the maximum Gr_x peak increases with the Reynolds number, while varying the free-stream turbulence has negligible effects in this sense. Varying the Reynolds number is expected to provoke changes in the stability characteristics of the boundary layer detaching from the wall.[56] Nevertheless, the growth rate of disturbances was seen to not scale with any of the BL parameters at the point of separation. This is due to the geometry-induced separation considered here, which is expected to have different scaling properties compared to the pressure-induced one. More specifically, the separation position is determined by the leading-edge curvature and the incidence angle, while it does not depend on the local characteristics of the boundary layer.

The highest Gr_x value, as identified by the present DMD procedure, was seen to occur at the location where K–H rolls exhibit spanwise distortion and breakup. To clarify this observation, Fig. 14 presents a top view of instantaneous iso-surfaces of wall-normal velocity fluctuations for the case $Re = 1725$ and $Tu = 2.3\%$, along with the

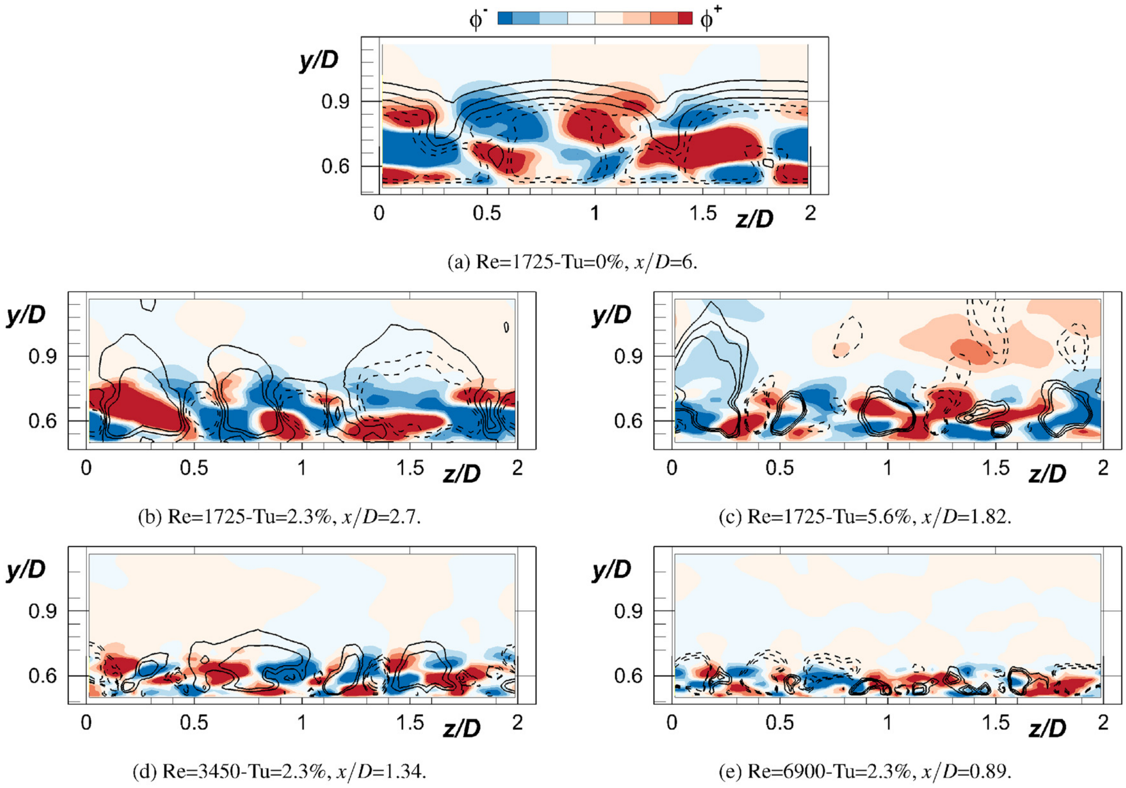

FIG. 15. Contour plot of real part of spanwise component of normalized DMD modes corresponding to the maximum Gr_x. Iso-contour lines of the wall-normal component of the modes are shown: solid and dashed lines indicate positive and negative values, respectively.

position of the maximum (Gr_x) peak. Additionally, the contour plot of the spanwise fluctuating velocity in a wall-parallel plane within the separated shear layer is included. The DMD analysis indicates that the maximum Gr_x value is reached at the location where at least one complete wavelength (l_x) of the spanwise vortices has developed. Once K–H rolls form near the maximum height of the bubble, they are seen to become unstable, displaying alternating contraction and expansion in the spanwise direction, along with sinuous-like motions in the cross-flow direction. This leads to an increase in the spanwise fluctuating velocity component, which contributes significantly to the overall amplification of disturbances in the LSB.

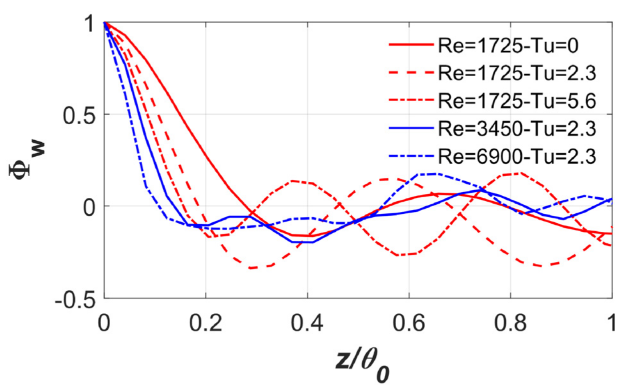

FIG. 16. Spanwise autocorrelation function (ACF) of the spanwise component of DMD modes (Φ_w).

Previous applications of the DMD procedure to 2D data, focusing solely on the streamwise and wall-normal velocity components,[57] identified the maximum instability in an LSB as being linked to the formation of K–H rolls. By incorporating spanwise fluctuations into the DMD kernel, the amplification of disturbances associated with the successive instability of K–H rolls is better captured. Indeed, cross-flow fluctuations become significant after the initial 2D rolls undergo distortion and subsequently break down, as illustrated in Fig. 14. Based on the current and previous literature studies,[48] two regions of pronounced instability in a laminar separation bubble can be identified. The first region, located near the bubble maximum displacement, is responsible for the formation of K–H rolls and the growth of streamwise and wall-normal fluctuations. The second region corresponds to the successive instability and breakup of spanwise rolls, resulting in the amplification of all three fluctuating velocity components. In addition to these processes, an initial stage of instability can be considered within the attached and separated shear layers, driving the formation and growth of streaky structures. This early instability stage is associated with the quasi-logarithmic growth of the root mean square of streamwise fluctuations, observed upstream of the regions where DMD predicts positive growth rate values (compare Figs. 7 and 13).

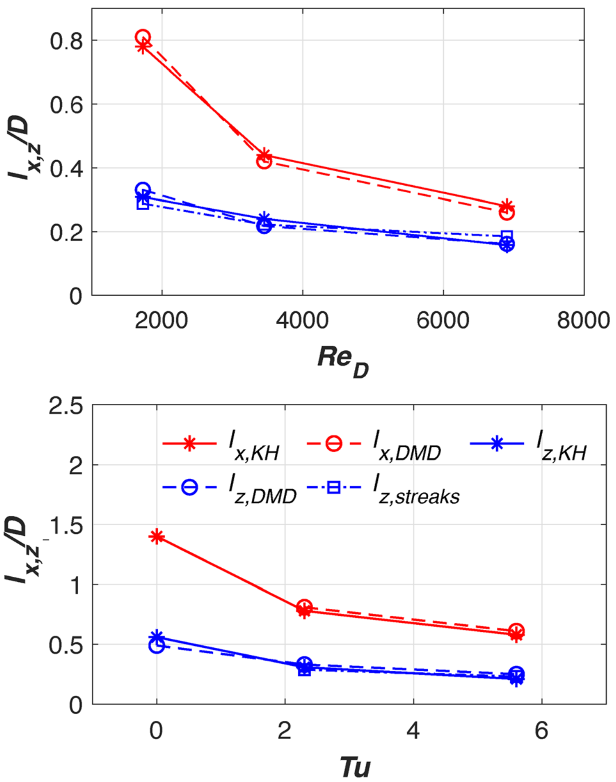

FIG. 17. (Top) Re and (bottom) *Tu* effect on K–H streaks and DMD-derived streamwise and spanwise wavelengths.

The optimal perturbations provided by the DMD algorithm are representative of the most unstable eigenmodes of the linearized Navier–Stokes operator. Consequently, the transient, non-modal growth of fluctuations responsible for the formation of streaky structures cannot be captured by the current procedure. However, streaks were seen to strongly perturb the separated shear layer (see Fig. 12), and they will be shown to play a key role in defining the most unstable spanwise modes that characterize the breakup process of Kelvin–Helmholtz rolls.

Figure 15 illustrates the effects of varying the Reynolds number and the turbulence intensity level on the spanwise and the wall-normal components of the most unstable DMD modes. These components are shown as they are directly associated with the formation and breakup of Kelvin–Helmholtz rolls. The modes corresponding to the highest Gr_x peak (see Fig. 13) are reported for each case. Consequently, modes are plotted at different streamwise positions due to the modification of the time-averaged structure of the laminar separation bubble. At the position of highest instability, the DMD modes exhibit an almost periodic pattern. The spanwise component alternates in sign across the cross-flow and wall-normal directions, while a similar cross-flow variation is observed in the wall-normal component of the modes. The spanwise variation of the wall-normal velocity component indicates the loss of bi-dimensionality of the K–H rolls, which were shown to exhibit both sinuous- and varicose-like motions before they break up. In addition to this, the patterns highlighted by the modes are consistent with the formation of a localized streamwise vorticity field that may cause the disruption of the K–H rolls.

Figure 16 reports the autocorrelation function (ACF) of the spanwise component of the modes depicted in Fig. 15. The autocorrelation function of Φ_w in the z-direction is defined in discrete form as

$$ACF[z_k] = \frac{1}{var_z(\Phi_w)} \sum_{n=1}^{N_z-k} \Phi_w[z_n]\Phi_w[z_{n+k}]. \tag{6}$$

Here, $var_z(\Phi_w)$ denotes the variance of Φ_w sampled along the spanwise direction at fixed x and y positions, n is the index of the local spanwise position, and k is the index corresponding to the spanwise lag at which ACF is computed. $ACF[z_k]$ is a function of only $[z_k]$ and it provides the degree of self-similarity of the mode from $z/D = 0$ to $z/D = D_z$. The first negative peak observed in Fig. 16 for the different cases corresponds to half of the spanwise wavelength characterizing the DMD modes shown in Fig. 15. This is the wavelength of the streamwise vortices forming in the contraction and expansion regions of K–H rolls, causing their disruption and the consequent turbulent reattachment. The spanwise scale captured by the modes is shown to reduce with increasing *Re* and the *Tu* level, following the reduction of the LSB dimensions.

To investigate the existing correlation between K–H roll and streak scales and the streamwise and spanwise wavelengths provided by the DMD procedure, Fig. 17 compares the variation of the most amplified streamwise ($l_{x,DMD}$) and spanwise ($l_{z,DMD}$) wavelengths, to those of boundary layer structures. The spanwise wavelength of streaky structures was computed by means of the spanwise ACF of the streamwise fluctuating velocity component in the fore part of the LSB. Differently, the streamwise wavelength of K–H rolls was obtained from the principal component analysis of the wall-normal velocity fluctuations,[58] not shown here for brevity. All flow scales reduce as *Re* and the *Tu* level increase. More noticeably, a marked correlation exists between streaks and K–H roll scales. The most amplified spanwise wavelength provided by the DMD algorithm ($l_{z,DMD}$) is shown to be the same as that of unstable K–H rolls ($l_{z,KH}$) and of laminar streaks ($l_{z,streaks}$).[16] Similarly, the most unstable streamwise scale ($l_{x,DMD}$) is the same as that of K–H rolls ($l_{x,KH}$). Streaks are therefore expected to play an active role in spanwise oscillation of K–H rolls preceding their breakup and transition. Overall, the correlation among the scales of the flow structures concurring to the boundary layer transition in a laminar separation bubble is shown to hold for different values of the Reynolds numbers and the *Tu* level.

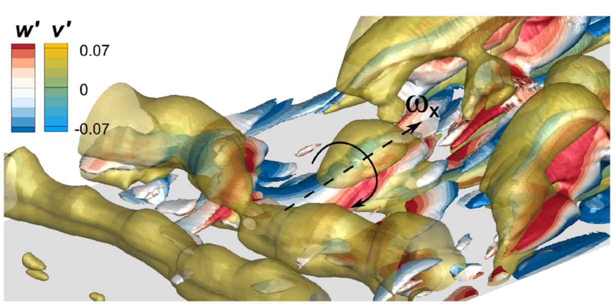

FIG. 18. Iso-surface at $v' = 0.05\,\mathrm{m/s}$ colored by v' and iso-surface of streamwise helicity at $H_x = 0.4\,\mathrm{m/s^2}$ colored by w' for the case $Re = 1725$ to $Tu = 2.3\%$.

C. The role of streaks in enhancing the local streamwise vorticity field

As mentioned above, the distributions of the spanwise and wall-normal velocity components highlighted by the DMD modes depicted in Fig. 15 can be seen as representative of streamwise vortices, which originate in the region of K–H roll instability. To investigate the occurrence of such a flow pattern, the streamwise contribution to the helicity field was computed, which is defined as the product between the streamwise vorticity and the streamwise velocity component, i.e., $H_x = \omega_x \times u$. Large values of H_x indicate regions where streamwise vorticity interacts with local streamwise momentum, promoting vorticity transport and the potential formation of streamwise vorticity tubes. Such flow patterns are expected to enhance distortion and breakup of K–H rolls, as suggested by the mode shapes reported in Fig. 15. Figure 18 shows the instantaneous iso-surface of wall-normal velocity fluctuations alongside the iso-surface of H_x for the case $Re = 1725$ and $Tu = 2.3\%$. The H_x iso-surface is colored by the instantaneous spanwise velocity fluctuations, w'. When a K–H roll undergoes distortion, H_x increases significantly, leading to its disruption. The local distribution of spanwise fluctuations reveals alternating positive and negative values of this velocity component in the cross-flow direction, as depicted by the DMD modes (Fig. 15). The unstable patterns captured by the modes are therefore consistent with the instability of the initially 2D K–H rolls (which carry mostly spanwise vorticity) due to the formation of localized regions with high streamwise rotation.

To further highlight the relationship between the occurrence of streaky structures and the enhancement of the streamwise vorticity field, the transport equation of the streamwise vorticity component (ω_x) is analyzed to show what terms may be affected by the occurrence of laminar streaks. The ω_x transport equation reads as follows:

$$\begin{aligned}\frac{\partial \omega_x}{\partial t} + u\frac{\partial \omega_x}{\partial x} + v\frac{\partial \omega_x}{\partial y} + w\frac{\partial \omega_x}{\partial z} &= \omega_x\frac{\partial u}{\partial x} + \omega_y\frac{\partial u}{\partial y} + \omega_z\frac{\partial u}{\partial z} \\ &\quad + \nu\left(\frac{\partial^2 \omega_x}{\partial^2 x} + \frac{\partial^2 \omega_x}{\partial^2 y} + \frac{\partial^2 \omega_x}{\partial^2 z}\right). \end{aligned} \tag{7}$$

Here, u, v, and w represent the velocity components in the x-, y-, and z-directions, respectively. In a first-order approximation, we neglected the diffusive terms based on the assumption that viscosity effects reduce as the boundary layer moves away from the wall. Equation (7) is then analyzed under the assumption of initially 2D K–H rolls in the region where their instability originates. In this context, ω_x and its wall-normal and spanwise derivatives are considered to be small; thus, the third and fourth terms on the left-hand side of Eq. (7) are neglected. The streamwise derivative of ω_x is instead retained since x is the direction of amplification of the streamwise vorticity. Equation (7) therefore assumes the following simplified form:

$$\frac{\partial \omega_x}{\partial t} + u\frac{\partial \omega_x}{\partial x} = \omega_x\frac{\partial u}{\partial x} + \omega_y\frac{\partial u}{\partial y} + \omega_z\frac{\partial u}{\partial z}. \tag{8}$$

The second term on the left-hand side of Eq. (8) can be rewritten as

$$u\frac{\partial \omega_x}{\partial x} = \frac{\partial (u\omega_x)}{\partial x} - \omega_x\frac{\partial u}{\partial x}, \tag{9}$$

where $u\omega_x$ is equal to H_x. Neglecting the streamwise derivatives of u, Eq. (8) becomes

$$\frac{\partial \omega_x}{\partial t} + \frac{\partial H_x}{\partial x} = \omega_y\frac{\partial u}{\partial y} + \omega_z\frac{\partial u}{\partial z}. \tag{10}$$

The left-hand side of Eq. (10) is the substantial derivative of ω_x, when this latter is supposed to grow solely in time and in the streamwise direction. Under the assumption of purely convective growth of ω_x, one may write $\partial\omega_x/\partial t = u\partial\omega_x/\partial x$, and the left-hand side of Eq. (10) might be further simplified to $2u\partial\omega_x/\partial x$. Regarding the terms appearing on the right-hand side of Eq. (10), those are seen to be affected by the occurrence of streaky structures. Indeed, regions of non-null ω_y typically originate between adjacent high- and low-speed streaks.[59] Once combined with the wall-normal shear term $(\partial u/\partial y)$ they lead to high values of the product $\omega_y \frac{\partial u}{\partial y}$. Similarly, streaky structures are characterized by well-defined spanwise wavelengths leading to periodic variation of the streamwise velocity component, i.e., $\frac{\partial u}{\partial z} \neq 0$. The presence of streaks therefore leads to non-negligible values of $\omega_z \frac{\partial u}{\partial z}$ in the regions where K–H rolls are formed, while this term is null in the case of pure 2D flows. According to Eq. (10), streaky structures forming in the separated shear layer therefore constitute an additional source of streamwise vorticity, whose growth was highlighted by the DMD modes as the possible cause of K–H roll instability.

VI. CONCLUSIONS

In this work, the most unstable modes of a laminar separation bubble forming at a flat plate leading edge were studied by means of high-fidelity numerical simulations and dynamic mode decomposition. Three Reynolds numbers and three free-stream turbulence levels were considered. For each flow case, DMD was computed over the streamwise coordinate so that the DMD eigenvalues identify streamwise waves that grow or decay in the flow direction. A local characterization of the unstable modes forming within an LSB was achieved by varying the streamwise extension of the DMD domain.

For the current Reynolds numbers, the boundary layer was seen to transition to turbulence at non-null free-stream turbulence conditions. The maximum amplification of fluctuations, as provided by the DMD algorithm, occurred at the streamwise positions where K–H rolls showed spanwise instability and initiated their breakup process. Spanwise sinuous motions as well as contractions and expansions of the rolls were seen to precede their breakup and transition. Based on the current and past works, three stages of streamwise instability can be identified in an LSB developing under the influence of free-stream turbulence. The first one leads to the formation and growth of streaky structures, being responsible for the logarithmic growth of streamwise fluctuations in the detached boundary layer.[18] Then, the second and third stages concern the formation and the successive breakup of spanwise rolls.[48] The current DMD-based analysis showed that the maximum growth rate of disturbances in an LSB occurs where the initial 2D K–H rolls get distorted, causing the amplification of all three fluctuating velocity components.

The wall-normal and spanwise components of the most unstable DMD modes were seen to describe the formation of streamwise vorticity regions in correspondence with the unstable K–H rolls. The inspection of the streamwise contribution to the helicity field revealed indeed the occurrence of streamwise vorticity tubes at the positions where K–H rolls break down to turbulence. The analysis of the simplified transport equation of the streamwise vorticity component showed that streaky structures enhance the generation of streamwise vorticity and the disruption of K–H rolls. The total derivative of streamwise vorticity was indeed shown to be influenced by:

- The combination of the wall-normal vorticity caused by alternating high- and low-speed streaks and the wall-normal gradient of the streamwise velocity component, i.e., $\omega_y \frac{\partial u}{\partial y}$.
- The combination of the spanwise gradient of the streamwise velocity component due to the presence of alternating high- and low-speed streaks and the local spanwise vorticity, i.e., $\omega_z \frac{\partial u}{\partial z}$. The quantity $\frac{\partial u}{\partial z}$ is linked to the time-mean wall-normal shear and to the occurrence of spanwise aligned 2D K–H rolls.

The comparison of the streamwise and spanwise scales of streaks and K–H rolls with those highlighted by the current DMD procedure showed that the most unstable spanwise wavelength of unstable rolls is the same as that of pre-transitional streaky structures. The results presented in this work indicate that streaks play an active role in promoting K–H roll breakup and transition in a laminar separation bubble under non-null free-stream turbulence levels.

ACKNOWLEDGMENTS

We acknowledge the CINECA award under the ISCRA initiative, for the availability of high-performance computing resources and support.

AUTHOR DECLARATIONS

Conflict of Interest

The authors have no conflicts to disclose.

Author Contributions

E. Canepa: Formal analysis (equal); Writing – original draft (equal). **A. Crivellini:** Data curation (equal); Resources (equal); Software (equal). **M. Dellacasagrande:** Conceptualization (lead); Formal analysis (lead); Methodology (lead); Writing – original draft (lead). **A. Ghidoni:** Data curation (equal); Formal analysis (equal); Resources (equal); Software (equal). **G. Noventa:** Data curation (lead); Resources (lead); Software (lead).

DATA AVAILABILITY

The data that support the findings of this study are available from the corresponding author upon reasonable request.

APPENDIX: NUMERICAL FRAMEWORK

In compact form the INS equations can be written as

$$\mathbf{P}\frac{\partial \mathbf{w}}{\partial t} + \nabla \cdot \mathbf{F}_c(\mathbf{w}) + \nabla \cdot \mathbf{F}_v(\mathbf{w}, \nabla \mathbf{w}) = \mathbf{0}, \tag{A1}$$

where m is the number of variables, d the number of dimensions, $\mathbf{w} = [p, u_i]^T \in \mathbb{R}^m$ the unknown solution vector, $\mathbf{F}_c, \mathbf{F}_v \in \mathbb{R}^m \otimes \mathbb{R}^d$ the convective and viscous flux functions. $\mathbf{P} = \mathbf{I} - \mathbf{J}^{11}$ is the difference between the identity and a single-entry matrix, $\mathbf{J}^{11}$, defined as the matrix with 1 at the $(1, 1)$ entry and zero elsewhere.

In the dG discretization, the weak form of Eq. (A1) is the result of a multiplication by an arbitrary test function and an integration by parts. The solution and the test function are then replaced with a finite element approximation and a discrete test function, which belong to $\mathbf{V}_h := [\mathbb{P}_d^k(\mathscr{K}_h)]^m$. $\mathbb{P}_d^k(\mathscr{K}_h) := \{v_h \in L^2(\Omega) \,|\, v_{h|K} \in \mathbb{P}_d^k(K), \forall K \in \mathscr{K}_h\}$ is the discrete polynomial space in physical coordinates, while $\mathbb{P}_d^k(K)$ is the restriction of the polynomial functions of d variables and degree at most k to the element K, part of the discretization $\mathscr{K}_h = \{K\}$ of the computational domain $\Omega \in \mathbb{R}^d$.

The discretization relies on a set of hierarchical and orthonormal basis functions defined in the physical space. For all the $K \in \mathscr{K}_h$ the basis $\Phi_K^k = \{\phi_i^K\}$, where $i \in \{1, \ldots, N_{dof}^K\}$, are computed with the application of the modified Gram–Schmidt (MGS) orthogonalization algorithm to a set of monomials defined in a reference space centered in the element barycenter and aligned with the principal axes of inertia of the element. The orthonormalization procedure can be expressed as the "composition" of the monomial basis with a set of coefficients for the MGS algorithm. Each component $j = 1, \ldots, m$ of the numerical solution $\mathbf{w}_h$ over any element K can be written, in terms of the elements of the global vector $\mathbf{W}$ of unknown degrees of freedom, as $\mathbf{w}_{h,j}^K = \phi_l^K W_{j,l}^K$, where $\mathbf{W}^K$ is the local part of the global vector of the degrees of freedom of the element K. The repeated index l implies summation over the $l = 1, \ldots, N_{dof}^K$. According to this notation, the dG discretization of the system in Eq. (A1) consists in the search, for $j = 1, \ldots, m$, of $\mathbf{W}$ such that

$$\begin{aligned} &\sum_{K \in \mathscr{T}_h} \int_K \phi_i^K P_{j,k}\, \phi_l^K \frac{dW_{k,l}^K}{dt} d\mathbf{x} \\ &\quad - \sum_{K \in \mathscr{T}_h} \int_K \frac{\partial \phi_i^K}{\partial x_n} F_{j,n}\big(\mathbf{w}_h, \nabla_h \mathbf{w}_h + \mathbf{r}([\![\mathbf{w}_h]\!])\big) d\mathbf{x} \\ &\quad + \sum_{F \in \mathscr{F}_h} \int_F [\![\phi_i^K]\!]\ {}_n\hat{F}_{j,n}\Big(\mathbf{w}_h^{\pm}, \big(\nabla_h \mathbf{w}_h + \eta_F \mathbf{r}_F([\![\mathbf{w}_h]\!])\big)^{\pm}\Big) d\sigma = 0, \end{aligned} \tag{A2}$$

for $i = 1, \ldots, N_{dof}^K$, where $\mathbf{F}$ is the sum of the convective and viscous flux functions, $\mathbf{n}$ is the unit vector normal to the boundary, $[\![\cdot]\!]$ and $\{\cdot\}$ are the jump and average trace operators, respectively. In Eq. (A2), repeated indices represent the summation over the ranges $k = 1, \ldots, m$, $l = 1, \ldots, N_{dof}^K$, $n = 1, \ldots, d$.

For the convective fluxes the discretization is based on the artificial compressibility flux of Bassi *et al.*[60] The main idea of the approach is to solve, at element interfaces, an exact Riemann problem associated with a local compressibility perturbation of the Euler equations. Since the perturbation is introduced only at the level of the flux calculation, no time derivative for the pressure variable is added to the discrete continuity equation, resulting in a time-consistent algorithm. Unlike other finite element methods, the same polynomial approximation is used for both velocity and pressure with a formal convergence rate of $k + 1$ and k, respectively. While for the viscous fluxes the discretization is based on the second scheme of Bassi and Rebay,[61] i.e., the BR2 scheme.

The numerical integration of Eq. (A2) via Gauss quadrature rules leads to a system of non-linear Differential Algebraic Equations (DAEs) that can be written as

$$\mathbf{M_P}\frac{d\mathbf{W}}{dt} + \mathbf{R}(\mathbf{W}) = \mathbf{0}, \tag{A3}$$

where $\mathbf{R}(\mathbf{W})$ is the vector of residuals of the spatial discretization and $\mathbf{M_P}$ is a global block diagonal matrix arising from the discretization of the first term in Eq. (A2). The choice of orthonormal basis functions allows reducing $\mathbf{M_P}$ to a modified identity matrix with zeros in the diagonal positions corresponding to the pressure degrees of freedom. The accurate time integration is based on the linearly implicit Rosenbrock-type Runge–Kutta schemes as

$$\mathbf{W}^{n+1} = \mathbf{W}^n + \sum_{j=1}^{s} m_j \mathbf{Y}_j, \tag{A4}$$

and

$$\left[\frac{\mathbf{M_P}}{\gamma\Delta t} + \frac{\partial \mathbf{R}(\mathbf{W}^n)}{\partial \mathbf{W}}\right]\mathbf{Y}_i = -\mathbf{R}\left(\mathbf{W}^n + \sum_{j=1}^{i-1} a_{ij}\mathbf{Y}_j\right) + \frac{\mathbf{M_P}}{\Delta t}\sum_{j=1}^{i-1} c_{ij}\mathbf{Y}_j, \quad i = 1, \dots, s, \tag{A5}$$

where m_j, γ, a_{ij}, and c_{ij} are real coefficients, and s is the number of stages. Where, among the Rosenbrock schemes available in the literature,[62,63] ROS3P (third order, three stages) scheme of Lang and Verwer[39] is used in this work. The PETSc library[64] is used for linear solvers, here preconditioned GMRES methods, and to devise a pure MPI parallel implementation for arrays, matrices, and the communication among them.

The solution of the linear system through GMRES needs only the evaluation of a matrix–vector product at each linear iteration. The Matrix-Based (MB) GMRES approach calculates and stores both the complete implicit operator matrix and the preconditioner, while the MF approach approximates the matrix–vector products in Eq. (A5) as

$$\left[\frac{\mathbf{M_P}}{\gamma\Delta t} + \frac{\partial \mathbf{R}(\mathbf{W}^n)}{\partial \mathbf{W}}\right]\Delta\mathbf{W} \simeq \frac{\mathbf{G}(\mathbf{W}^n + h\Delta\mathbf{W}) - \mathbf{G}(\mathbf{W}^n)}{h}, \tag{A6}$$

where

$$h = \varepsilon\frac{\sqrt{1 + ||\mathbf{W}^n||_{L^2}}}{||\Delta\mathbf{W}||_{L^2}}, \quad \mathbf{G}(\mathbf{W}) = \frac{\mathbf{M_P}}{\gamma\Delta t}\mathbf{W} + \mathbf{R}(\mathbf{W}), \tag{A7}$$

h is a numerical perturbation,[34] and $\varepsilon = 10^{-9}$ an user defined parameter. The finite differentiation error decreases the efficiency of the algorithm only for small tolerances of the linear system solution when its residual norm gets close to h.[37] However, those tolerances are not suitable for real-life simulations, and the MF- or MB-GMRES approaches need the same number of iterations to reach the convergence. One of the main advantages of MF-GMRES is that the computational cost for the matrix assembly can be reduced with the approximation and/or "freezing" of the preconditioner for a user-defined number of iterations without affecting the accuracy of the time integration.

ALGORITHM 1. p-MG algorithm, i.e., $\breve{\mathbf{W}}_l = \mathrm{MG}(l, \mathbf{b}_l, \mathbf{W}_l)$. $\mathbf{I}_{l+1}^{l}$ and $\mathbf{I}_{l}^{l+1}$ are the prolongation and restriction operators, and $\mathbf{e}_{l+1}$ is the correction term.

```
if l = L then
   SOLVE A_l W̆_l = b_l
else
     W̆_l = SMOOTH(W_l, A_l, b_l, ν_1)
     r_l = b_l − A_l W̆_ℓ
     r_{l+1} = I_l^{l+1} r_l
     e_{l+1} = MG(l+1, r_{l+1}, 0)
     Ŵ_l = W̆_l + I_{l+1}^l e_{l+1}
     W̆_l = SMOOTH(Ŵ_l, A_l, b_l, ν_2)
end if
return W̆_l
```

Standard preconditioners for GMRES based on the factorization of the Jacobian matrix are the Additive Schwarz domain decomposition Method (ASM) preconditioner, the ILU decomposition Block Jacobi (BJ), and the Element-wise Block Jacobi (EWBJ). Unfortunately, iterative solvers based on these preconditioners are not able to reduce the linear system solution error when used to solve the INS equations. The error can be expressed as a combination of "modes," and standard preconditioners are able to damp efficiently, in few iterations, only the oscillatory part, while smooth modes are damped very slowly, resulting in a stall of the convergence. To speed up the linear system convergence, a linear multigrid (MG) algorithm is here used as a preconditioner for MF-GMRES. The use of MF-GMRES is mandatory since the action of the preconditioner changes at each time step, and it needs to be stored in memory to compute accurately the final solution using Krylov subspaces.

The basic idea of MG is to use coarser solutions to smooth separately all the modes of the error. In fact, low-frequency modes on coarser solutions become part of the high-frequency range and can be damped by standard iterative smoothers. In p-MG, the fine solution is accelerated by computing corrections with coarser solutions with the prolongation and the restriction of the solution between different approximations, or grids. Algorithms 1 and 2 show the p-MG algorithm based on a V-cycle used in this work. Any coarse problem of Eq. (A5) can be written in compact form as $\mathbf{A}_l\mathbf{W}_l = \mathbf{b}_l$, where $\mathbf{A}_l$ is the restriction to level l of the finest level matrix, $\mathbf{W}_l$ is the vector of the coefficients of the unknown polynomial functions on the coarse level l and $\mathbf{b}_l$ is the restriction of the finest level right-hand side (RHS). Furthermore, L is the number of multigrid levels with $l = 1, \dots, L$, where $l = 1$ and $l = L$ represent the finest and coarsest levels, respectively. ν_1 pre-smoothing iterations are carried out at each level before the restriction of the solution to the coarser level. While on the way back to the finest level, ν_2 post-smoothing iterations are carried out at each level after the correction of the solution with the prolonged term. In the Full-MG (FMG) algorithm the V-cycle is called in each level starting from the coarsest, where at the end of each cycle the solution is prolonged to the next fine level.

Several parameters of the FMG algorithm are user-defined: the number of multigrid levels, the solution approximation of the coarse

ALGORITHM 2. Full *p*-MG (FMG) algorithm.

for $l = L, 1, -1$ **do**
  if $l = L$ **then**
    $\mathbf{b}_l = \mathbf{I}_1^l \mathbf{b}_1$
    SOLVE $\mathbf{A}_l \mathbf{W}_l^{\mathrm{FMG}} = \mathbf{b}_l$
  else
    $\mathbf{b}_l = \mathbf{I}_1^l \mathbf{b}_1$
    $\tilde{\mathbf{W}}_l = \mathbf{I}_{l+1}^l \mathbf{W}_{l+1}^{\mathrm{FMG}}$
    $\mathbf{W}_l^{\mathrm{FMG}} = \mathrm{MG}(l, \mathbf{b}_l, \tilde{\mathbf{W}}_l)$
  end if
end for
return $\mathbf{W}_l^{\mathrm{FMG}}$

levels, the smoother and preconditioner for each level, and the tolerances. As suggested by previous works,[34,37] the MF-GMRES smoother coupled with an EWBJ preconditioner is used on all the levels, up to $k = 6$, to reduce the memory footprint with a maximum number of GMRES iteration $n_{it}^{max} = 8$, and the MB-GMRES smoother with an ASM preconditioner is used on the coarsest level, i.e., $k = 1$, to improve the convergence with a maximum number of GMRES iteration $n_{it}^{max} = 60$.

Bassi *et al.*[34] proved the effectiveness of this time integration on one of the configurations of this work, i.e., T3L1. The results of the comparison between *p*-MG and other approaches, e.g., BJ-MB, ASM-MB, BF-MF, and EWBJ-MF, spotlighted that *p*-MG reduces the computational time by $\sim$50% and the memory footprint by 85% with respect to a standard MB approach. Thanks to *p*-MG, the GMRES iterations are low even when the matrix operator is lagged over different time steps, without any significant influence on the memory footprint. The *p*-MG preconditioner in an MF-GMRES framework automatically keeps track in its structure of the solution changes even when the operator assembly is lagged. The lag of the operator assembly allows further improving the saving in terms of computational time, which is 69% lower than the value measured for a standard BJ-MB algorithm.

In these simulations the flow is very sensitive to the free-stream turbulence intensity, Tu, and the injection of the turbulence is of paramount importance. In fact, different turbulence intensities are here considered, e.g., $Tu = \{0.0\%, 0.2\%, 0.65\%, 2.3\%, 5.6\%\}$. Instead, the influence of the turbulence length scale is not considered due to the fact that the free-stream turbulence intensity, Tu, is calculated at the leading edge of the plate and the dissipation is negligible along the separation bubble whatever the turbulence length scale is. In other works, e.g., Yang and Voke,[38] Langari and Yang,[45] and Lamballais *et al.*,[46,47] a white-noise random perturbation is added at the inflow velocity to mimic the low experimental turbulence level, i.e., $Tu < 0.2\%$. While in this work the generation of turbulence far from the plate is not feasible due to aggressive mesh coarsening. In fact, the low spatial accuracy in the free stream would damp any random perturbation imposed upstream. As a consequence, the turbulent fluctuations are synthetically injected via a spatially supported random forcing term slightly upstream of the plate, where the spatial accuracy is enough to avoid the dissipation of the small-scale perturbation. The forcing term, $\mathbf{f}_h$, represents a source term in the discrete momentum equations. This approach, instead of perturbing the flow velocity directly, guarantees a divergence-free perturbation, consistent with the incompressibility constraint. The term is computed with the multiplication of a random three-dimensional discrete vector $\mathbf{r}_h$ to a function of the spatial coordinates x, y, and z. This function is chosen to be a Gaussian distribution in the x-direction and homogeneous in y and z such that

$$\sum_{K\in\mathscr{T}_h}\int_K \phi_i^K f_{h,j} d\mathbf{x} = \sum_{K\in\mathscr{T}_h}\int_K \phi_i^K \left(Ae^{-\left(\frac{x-\bar{x}}{2\alpha}\right)^2}\right) r_{h,j} d\mathbf{x},$$

where A, $\bar{x}$, and α are the amplitude coefficient, the streamwise coordinate of the plane, and the amplitude of the Gaussian distribution. The random vector $r_{h,j}$ is computed separately at each Gauss quadrature point during residual assembly and normalized so that $||\mathbf{r}_h|| = 1$. It should be noted that the discrete forcing vector changes not only in space but also in time. In this work, the Gaussian function is centered at $\bar{x}/D = -3$ and the constants A, α are adjusted by trial and error to match the experimental free-stream turbulent intensity, Tu, at the leading edge of the plate. This forcing term was the same as that of Bassi *et al.*,[34] Cimarelli *et al.*,[36] and Franciolini *et al.*[35]

REFERENCES

[1] J. W. Kurelek, B. A. Tuna, S. Yarusevych, and M. Kotsonis, "Three-dimensional development of coherent structures in a two-dimensional laminar separation bubble," AIAA J. **59**, 493–505 (2021).
[2] R. Kumar and S. Sarkar, "Features of laminar separation bubble subjected to varying adverse pressure gradients," Phys. Fluids **35**, 124104 (2023).
[3] J. Smith, G. Pisetta, and I. M. Viola, "The scales of the leading-edge separation bubble," Phys. Fluids **33**, 045101 (2021).
[4] X. Fang and M. F. Tachie, "Spatio-temporal dynamics of flow separation induced by a forward-facing step submerged in a thick turbulent boundary layer," J. Fluid Mech. **892**, A40 (2020).
[5] I. Tani, "Low-speed flows involving bubble separations," Prog. Aerosp. Sci. **5**, 70–103 (1964).
[6] S. Hosseinverdi and H. F. Fasel, "Numerical investigation of laminar–turbulent transition in laminar separation bubbles: The effect of free-stream turbulence," J. Fluid Mech. **858**, 714–759 (2019).
[7] O. Marxen, M. Lang, and U. Rist, "Vortex formation and vortex breakup in a laminar separation bubble," J. Fluid Mech. **728**, 58–90 (2013).
[8] A. Sengupta and P. Tucker, "Effects of forced frequency oscillations and free stream turbulence on the separation-induced transition in pressure gradient dominated flows," Phys. Fluids **32**, 104105 (2020).
[9] M. Dellacasagrande, D. Lengani, D. Simoni, M. Ubaldi, and P. Zunino, "Evaluation of turbulent spot production rate in boundary layers under variable pressure gradients for gas turbine applications," J. Turbomach. **142**, 061003 (2020).
[10] M. Dellacasagrande, D. Barsi, D. Lengani, and D. Simoni, "Instability processes in short and long laminar separation bubbles," Exp. Fluids **65**, 109 (2024).
[11] S. Hosseinverdi, W. Balzer, and H. Fasel, "Direct numerical simulations of the effect of free-stream turbulence on 'long' laminar separation bubbles," in *42nd AIAA Fluid Dynamics Conference and Exhibit* (AIAA, 2012), p. 2972.
[12] J. H. M. Fransson and S. Shahinfar, "On the effect of free-stream turbulence on boundary-layer transition," J. Fluid Mech. **899**, A23 (2020).
[13] T. Zaki, "From streaks to spots and on to turbulence: Exploring the dynamics of boundary layer transition," Flow Turbul. Combust. **91**, 451–473 (2013).
[14] O. Marxen and T. A. Zaki, "Turbulence in intermittent transitional boundary layers and in turbulence spots," J. Fluid Mech. **860**, 350–383 (2019).
[15] S. Lardeau, M. Leschziner, and T. Zaki, "Large eddy simulation of transitional separated flow over a flat plate and a compressor blade," Flow Turbul. Combust. **88**, 919–944 (2012).

[16]J. Verdoya, M. Dellacasagrande, D. Lengani, D. Simoni, and M. Ubaldi, "Inspection of structures interaction in laminar separation bubbles with extended proper orthogonal decomposition applied to multi-plane particle image velocimetry data," Phys. Fluids **33**, 043607 (2021).
[17]D. Simoni, D. Lengani, M. Ubaldi, P. Zunino, and M. Dellacasagrande, "Inspection of the dynamic properties of laminar separation bubbles: Free-stream turbulence intensity effects for different Reynolds numbers," Exp. Fluids **58**, 66 (2017).
[18]M. S. Istvan, J. W. Kurelek, and S. Yarusevych, "Turbulence intensity effects on laminar separation bubbles formed over an airfoil," AIAA J. **56**, 1335–1347 (2018).
[19]S. M. Aniffa, V. Caesar, V. Dabaria, and A. Mandal, "Characteristics of geometry-and pressure-induced laminar separation bubbles at an enhanced level of free-stream turbulence," J. Fluid Mech. **957**, A19 (2023).
[20]P. J. Przytarski and A. P. Wheeler, "Accurate prediction of loss using high fidelity methods," J. Turbomach. **143**, 031008 (2021).
[21]M. Dellacasagrande and P. J. Przytarski, "Turbulence generation mechanisms in compressor boundary layers," in *Turbo Expo: Power for Land, Sea, and Air* (American Society of Mechanical Engineers, 2024), Vol. 88056, p. V12AT29A045.
[22]D. Rodriguez and V. Theofilis, "Structural changes of laminar separation bubbles induced by global linear instability," J. Fluid Mech. **655**, 280–305 (2010).
[23]L. Jones, R. Sandberg, and N. Sandham, "Direct numerical simulations of forced and unforced separation bubbles on an airfoil at incidence," J. Fluid Mech. **602**, 175–207 (2008).
[24]S. S. Diwan and O. Ramesh, "Relevance of local parallel theory to the linear stability of laminar separation bubbles," J. Fluid Mech. **698**, 468–478 (2012).
[25]D. Borgmann, S. Hosseinverdi, J. C. Little, and H. F. Fasel, "Investigation of laminar separation bubbles using experiments, theory and DNS," in *AIAA Aviation 2021 Forum* (AIAA, 2021), p. 2898.
[26]C. Toppings and S. Yarusevych, "Linear stability analysis of a three-dimensional laminar separation bubble on a finite wing," Int. J. Heat Fluid Flow **101**, 109141 (2023).
[27]D. Lengani, D. Simoni, M. Ubaldi, P. Zunino, and F. Bertini, "Experimental study of free-stream turbulence induced transition in an adverse pressure gradient," Exp. Therm. Fluid Sci. **84**, 18–27 (2017).
[28]J. Weiss, B. Steinfurth, L. Chamard, A. Giani, and P. Combette, "Spectral proper orthogonal decomposition of unsteady wall shear stress under a turbulent separation bubble," AIAA J. **60**, 2150–2159 (2022).
[29]T.-K. Wang and K. Shoele, "Kernel mode decomposition for time-frequency localization of transient flow: The formation of a laminar separation bubble," Phys. Rev. Fluids **8**, 064401 (2023).
[30]C. Ye, C. Wang, H. Yan, F. Wang, Y. Zheng, B. van Esch *et al.*, "Investigation on transition characteristics of laminar separation bubble on a hydrofoil," Phys. Fluids **35**, 105154 (2023).
[31]S. Priebe, J. H. Tu, C. W. Rowley, and M. P. Martín, "Low-frequency dynamics in a shock-induced separated flow," J. Fluid Mech. **807**, 441–477 (2016).
[32]W. Wu, C. Meneveau, and R. Mittal, "Spatio-temporal dynamics of turbulent separation bubbles," J. Fluid Mech. **883**, A45 (2020).
[33]J. Coupland and D. Brierley, "Transition in turbomachinery flows," Final report (Measurements available at the ERCOFTAC site, 1996).
[34]F. Bassi, L. Botti, A. Colombo, A. Crivellini, M. Franciolini, A. Ghidoni, and G. Noventa, "A p-adaptive Matrix-Free Discontinuous Galerkin method for the implicit LES of incompressible transitional flows," Flow Turbul. Combust. **105**, 437–470 (2020).
[35]M. Franciolini, L. Botti, A. Colombo, and A. Crivellini, "p-multigrid matrix-free discontinuous Galerkin solution strategies for the under-resolved simulation of incompressible turbulent flows," Comput. Fluids **206**, 104558 (2020).
[36]A. Cimarelli, M. Franciolini, and A. Crivellini, "Numerical experiments in separating and reattaching flows," Phys. Fluids **32**, 095119 (2020).
[37]M. Franciolini, A. Crivellini, and A. Nigro, "On the efficiency of a matrix-free linearly implicit time integration strategy for high-order discontinuous Galerkin solutions of incompressible turbulent flows," Comput. Fluids **159**, 276–294 (2017).
[38]Z. Yang and P. R. Voke, "Large-eddy simulation of boundary-layer separation andtransition at a change of surface curvature," J. Fluid Mech. **439**, 305–333 (2001).
[39]J. Lang and J. Verwer, "ROS3P—An accurate third-order Rosenbrock solver designed for parabolic problems," BIT Numer. Math. **41**, 731–738 (2001).
[40]P. J. Schmid, "Dynamic mode decomposition of numerical and experimental data," J. Fluid Mech. **656**, 5–28 (2010).
[41]P. J. Schmid, "Dynamic mode decomposition and its variants," Annu. Rev. Fluid Mech. **54**, 225–254 (2022).
[42]J. N. Kutz, S. L. Brunton, B. W. Brunton, and J. L. Proctor, *Dynamic Mode Decomposition: Data-Driven Modeling of Complex Systems* (SIAM, 2016), Vol. 149.
[43]J. Coupland and D. Brierley, "Transition in turbomachinery flows," Final Report, BRITE/EURAM Project AERO-CT92-0050 (1996).
[44]A. Palikaras, K. Yakinthos, and A. Goulas, "The effect of negative shear on the transitional separated flow around a semi-circular leading edge," Int. J. Heat Fluid Flow **24**, 421–430 (2003).
[45]M. Langari and Z. Yang, "Numerical study of the primary instability in a separated boundary layer transition under elevated free-stream turbulence," Phys. Fluids **25**, 074106 (2013).
[46]E. Lamballais, J. Silvestrini, and S. Laizet, "Direct numerical simulation of a separation bubble on a rounded finite-width leading edge," Int. J. Heat Fluid Flow **29**, 612–625 (2008).
[47]E. Lamballais, J. Silvestrini, and S. Laizet, "Direct numerical simulation of flow separation behind a rounded leading edge: Study of curvature effects," Int. J. Heat Fluid Flow **31**, 295–306 (2010).
[48]A. Alessandri, P. Bagnerini, M. Gaggero, D. Lengani, and D. Simoni, "Dynamic mode decomposition for the inspection of three-regime separated transitional boundary layers using a least squares method," Phys Fluids **31**, 044103 (2019).
[49]M. S. Istvan and S. Yarusevych, "Effects of free-stream turbulence intensity on transition in a laminar separation bubble formed over an airfoil," Exp. Fluids **59**, 52 (2018).
[50]M. Dellacasagrande, D. Lengani, E. Bertolini, and W. Sanz, "Correlated pressure–velocity instability in a transonic high-pressure turbine blade," J. Turbomach. **145**, 041015 (2023).
[51]M. Dellacasagrande, D. Barsi, D. Lengani, D. Simoni, and J. Verdoya, "Response of a flat plate laminar separation bubble to Reynolds number, free-stream turbulence and adverse pressure gradient variation," Exp. Fluids **61**, 128 (2020).
[52]M. Alam and N. Sandham, "Direct numerical simulation of 'short' laminar separation bubbles with turbulent reattachment," J. Fluid Mech. **410**, 1–28 (2000).
[53]E. Eljack, J. Soria, Y. Elawad, and T. Ohtake, "Simulation and characterization of the laminar separation bubble over a NACA-0012 airfoil as a function of angle of attack," Phys. Rev. Fluids **6**, 034701 (2021).
[54]S. Sarmast, R. Dadfar, R. F. Mikkelsen, P. Schlatter, S. Ivanell, J. N. Sørensen, and D. S. Henningson, "Mutual inductance instability of the tip vortices behind a wind turbine," J. Fluid Mech. **755**, 705–731 (2014).
[55]M. Dellacasagrande, D. Lengani, D. Simoni, J. Pralits, K. Durovich, A. Hanifi, and D. Henningson, "Statistical characterization of free-stream turbulence induced transition under variable Reynolds number, free-stream turbulence, and pressure gradient," Phys. Fluids **33**, 094115 (2021).
[56]A. Dotto, M. Luzzi, J. Verdoya, D. Simoni, A. Hanifi, and J. O. Pralits, "Stability of low-pressure turbine boundary layers under variable Reynolds number and pressure gradient," Phys. Fluids **36**, 034116 (2024).
[57]M. Dellacasagrande, J. Verdoya, D. Barsi, D. Lengani, and D. Simoni, "Dynamic mode decomposition analysis of separated boundary layers under variable Reynolds number and free-stream turbulence," in *Turbo Expo: Power for Land, Sea, and Air* (American Society of Mechanical Engineers, 2020), Vol. 84102, p. V02ET41A038.
[58]D. Lengani, D. Simoni, M. Ubaldi, and P. Zunino, "POD analysis of the unsteady behavior of a laminar separation bubble," Exp. Therm. Fluid Sci. **58**, 70–79 (2014).
[59]M. Dellacasagrande, D. Lengani, D. Simoni, J. Pralits, K. Durović, A. Hanifi, and D. Henningson, "A procedure for computing the spot production rate in transitional boundary layers," Exp. Fluids **63**, 136 (2022).
[60]F. Bassi, A. Crivellini, D. Di Pietro, and S. Rebay, "An artificial compressibility flux for the discontinuous Galerkin solution of the incompressible Navier–Stokes equations," J. Comput. Phys. **218**, 794–815 (2006).
[61]F. Bassi and S. Rebay, "A high order discontinuous Galerkin method for compressible turbulent flows," in *Discontinuous Galerkin Methods*, edited by B.

Cockburn, G. E. Karniadakis, and C.-W. Shu (Springer Berlin Heidelberg, Berlin, Heidelberg, 2000), pp. 77–88.
[62] G. Noventa, F. Massa, S. Rebay, F. Bassi, and A. Ghidoni, "Robustness and efficiency of an implicit time-adaptive discontinuous Galerkin solver for unsteady flows," Comput. Fluids **204**, 104529 (2020).
[63] F. Massa, G. Noventa, M. Lorini, F. Bassi, and A. Ghidoni, "High-order linearly implicit two-step peer schemes for the discontinuous Galerkin solution of the incompressible Navier–Stokes equations," Comput. Fluids **162**, 55–71 (2018).
[64] S. Balay, S. Abhyankar, M. F. Adams, J. Brown, P. Brune, K. Buschelman, L. Dalcin, A. Dener, V. Eijkhout, W. D. Gropp, D. Karpeyev, D. Kaushik, M. G. Knepley, D. A. May, L. C. McInnes, R. T. Mills, T. Munson, K. Rupp, P. Sanan, B. F. Smith, S. Zampini, H. Zhang, and H. Zhang, see https://www.mcs.anl.gov/petsc for "PETSc Web page" (2019).